Carbon 228 (2024) 119426

Contents lists available at ScienceDirect

Carbon

journal homepage: www.elsevier.com/locate/carbon

# Estimation of soot refractive index from its nanostructural parameters with the dispersion model

Sofía González-Correa [a], David Bolonio [b], Rosario Ballesteros [a], Magín Lapuerta [a,*]

[a] E.T.S. Ingeniería Industrial. Universidad de Castilla-La Mancha, Avda. Camilo José Cela s/n., 13071, Ciudad Real, Spain
[b] Department of Energy & Fuels, ETS Ingenieros de Minas y Energía, Universidad Politécnica de Madrid. Ríos Rosas 21, 28003, Madrid, Spain

ARTICLE INFO

*Keywords:*
Soot
Agglomerates
Refractive index
Graphite
X ray diffraction
Raman spectroscopy

ABSTRACT

Particles derived from combustion processes, mainly composed of soot agglomerates, are acknowledged to be among the main contributors to climate change. Their effects depend mostly on their size, shape, and internal structure. Specifically, the latter has a significant effect on their optical properties, mainly through the refractive index. This index has been widely evaluated, but scarcely correlated with the soot internal characteristics. In this work, relationships between the nanostructural parameters (such as the degree of graphitization, among others) obtained with conventional analytical techniques and the input parameters of the dispersion model (a representation of the electromagnetic radiation through the Lorentz-Drude approach) are proposed with the aim to determine the refractive index. From experiments in a chassis dynamometer, it has been observed that as the vehicle speed increases, the soot samples have, in general, higher degree of graphitization, due to increased combustion temperature. The method proposed allows quantifying how both the real and imaginary parts of the complex refractive index increase as the degree of graphitization increases. Much lower dependence on the average crystal length has been observed. Different combinations of techniques can be used to determine the nanostructural parameters, depending on the analytical technique used. As far as the resulting parameters are reliable, the effect of the technique selected is minor, thus providing flexibility to the application of the method.

## 1. Introduction

Particle aerosols from combustion processes are acknowledged to be among the main contributors to climate change, as far as they can absorb or scatter considerable amount of sunlight at different wavelengths [1]. In fact, very disperse values of Global Warming Potential (GWP) have been proposed for combustion-derived particles [2]. However, the quantification of their effect is much more difficult than that of gases, because the optical and radiative properties of soot agglomerates depend on their chemical composition, size, shape, and internal structure [3]. Discussions about the role of soot particles on the radiative forcing come from long ago [4], but up to date, no scientific methodology has been proposed to quantify such role considering all variables.

Particles derived from combustion processes are mainly composed of soot agglomerates (usually denoted as black carbon by environmentalists) with a wide distribution of sizes located in the submicron range, although they can also be composed of hydrocarbons adsorbed on the soot surface (in this case often denoted as brown carbon). Black carbon and brown carbon have different spectral optical properties [5]. Small aerosol particles have high absorption efficiencies, with a consequent dominating heating effect, whereas larger aerosol particles have high scattering efficiencies, with a dominating cooling effect [1]. Similarly, for equal size, irregular and cluster-shaped particles (with low fractal dimension) have higher absorption efficiencies, thus contributing to the heating effect, whereas more compact particles (with higher fractal dimensions) have higher scattering efficiencies, contributing to cool the lowest layers of the atmosphere [6]. Also, they have different atmospheric residence times depending on their size and shape. Finally, the internal graphite-like structure of soot particles has also significant effect on the optical behaviour of agglomerates [7]. More graphitic particles have higher complex refractive index (i.e., both the real and imaginary parts are higher) than more disordered soot.

The complex refractive index ($m = n + ik$) describes how the matter responds to the electromagnetic field [5]. Since its effect on the optical behaviour of particles is huge, a precise determination of this parameter is essential. Many authors have proposed soot refractive index values at specific wavelengths such as the value of 1.95–0.79$i$ (at 550 nm) proposed by Bond & Bergstrom [8], or other proposed values collected in

* Corresponding author.
*E-mail address:* magin.lapuerta@uclm.es (M. Lapuerta).

https://doi.org/10.1016/j.carbon.2024.119426
Received 7 February 2024; Received in revised form 27 June 2024; Accepted 6 July 2024
Available online 6 July 2024

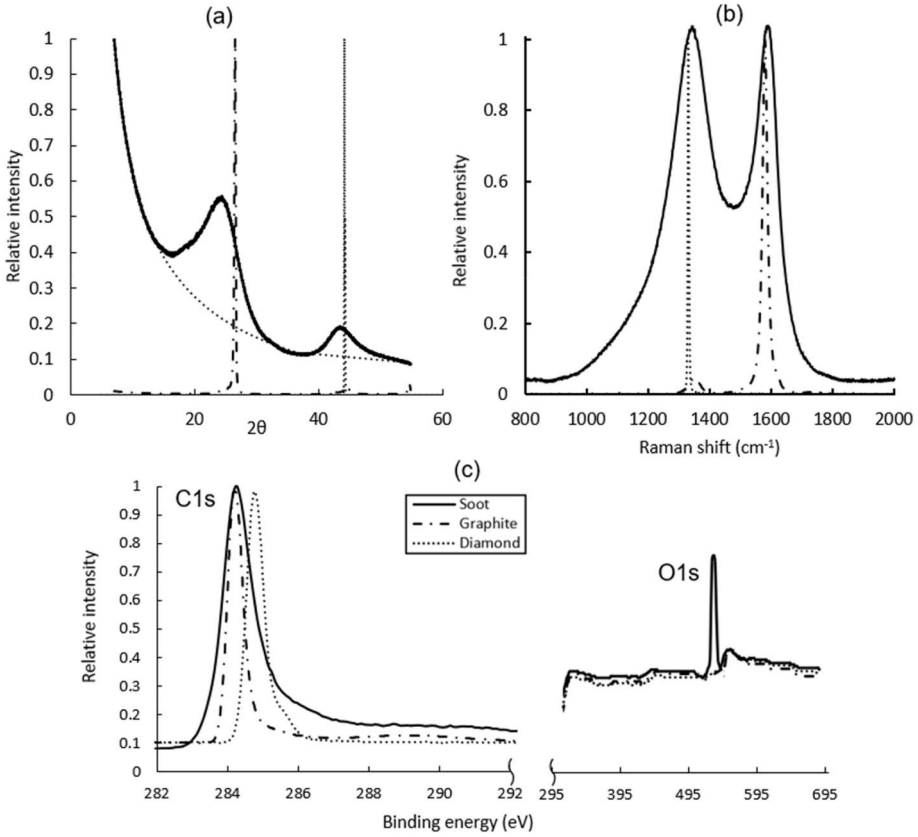


**Fig. 1.** Examples of typical XRD (a), Raman spectroscopy (b), and XPS (c) for soot (solid line), graphite (dot-dashed line), and diamond (dashed line) [23,24,33].

the review by Liu et al. [9]. However, the wavelength-dependence must be considered for precise spectral simulations. Different techniques like indirect measurements from light reflectance or light attenuation have been used to determine the refractive index [10,11], as well as modelling methods such as the effective medium models [12,13] or correlations based on experimental results [14–16]. One of the most widely used methods to determine the complex refractive index of a material is the dispersion model [7,17,18]. This model simulates the complex dielectric constant or relative dielectric constant ($\varepsilon$), which is a macroscopic variable describing how the electric charge of a material is distorted in the presence of an electric field [19]. In practice, determining the dielectric constant is equivalent to determine the refractive index, since they are related through the Maxwell relation ($\varepsilon = m^2$), which originally related their real parts and was valid for transparent materials, but was later extended to their complex forms with the aim to extend its validity to all kinds of materials [20].

However, it has been observed that the complex refractive index depends on the composition and internal structure of soot [7,21], quantified by means of parameters such as the interlayer distance ($d_{002}$), the length of the graphitic crystals ($L_a$), or the type of carbon bonds. Soot can be formed by $sp^2$ and $sp^3$ bonds. $sp^2$ bonds indicate similarity with graphite and are most abundant in soot, thus allowing to quantify a degree of graphitization for soot ($G$). In addition, since it may have some presence of $sp^3$ bonds [22], a certain degree of diamantization ($D$) can also be defined. Both parameters can be obtained by various structural characterization techniques: X-Ray Diffraction (XRD), Transmission Electron Microscopy (TEM), Raman spectroscopy, X-ray Photoelectron Spectroscopy (XPS), and Atomic Force Microscopy (AFM).

X-Ray Diffraction provides information about the soot nanostructure through the diffraction patterns that are generated from the interaction between X-rays and the material. A typical soot diffraction pattern (solid line) is shown in Fig. 1a, in comparison with the pattern of highly oriented graphite (dot-dashed line) [23] and diamond (dashed line) [24]. As observed in Fig. 1a, soot shows two peaks (usually denoted as the 002 and 100 peaks, from the lower to the higher diffraction angle), whereas graphite has a main peak at 26° and diamond at 44° [24–26]. Using Scherrer equation, the crystal length can be determined [27] with the width of the 100 band [23], whereas the interlayer distance can be determined using Bragg's law based on the sine of the 002-diffraction angle.

Transmission Electron Microscopy images can be processed to determine the morphological characteristics of particles with a high level of detail, such as the primary particle size. In addition, the nanostructure of soot can be evaluated with high-resolution TEM (HRTEM), allowing to determine the interlayer distance, as well as with XRD. To better measure the nanostructural parameters from HRTEM images, the regions in the primary particles can be specified and cropped (in area of around 10 × 10 nm), after being converted into binary black and white images and finally transformed into skeletonized images [28].

Belenkov [29] showed that the interlayer distance of infinite crystals of graphite tends to 3.3796 Å and proposed this value as the limit for the theoretical spacing for pure graphite. For different soot types, values range between 3.5 and 3.7 [30,31]. Atria et al. [32] considered an arbitrary maximum spacing of 3.7 Å, above all the results observed by these authors, but below the interlayer spacing of exfoliated carbon fringes.

Raman spectra is commonly used to characterize disordered carbonaceous materials, since it is very sensitive to changes that break the translational symmetry, such as the lattice defects in soot [34]. The Raman spectrum typically obtained when analysing a soot sample (solid line) is shown in Fig. 1b, compared to the spectrum of graphite (dot--dashed line) and diamond (dashed line). In the soot spectrum two main bands can be distinguished: the G-band and the D-band. The G-band (right peak usually centred around 1580 $cm^{-1}$) is the response to the in-plane displacements associated with $sp^2$ bonds. The D-band (left peak usually centred around 1350 $cm^{-1}$ [33]), is the response to weaker

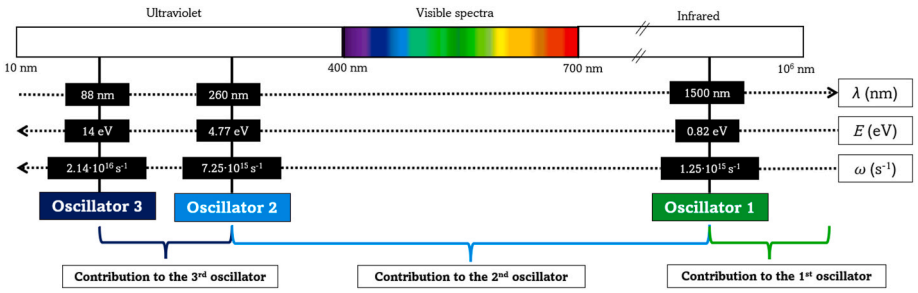


**Fig. 2.** Spectral ranges with contribution of electro-bound oscillators.

atomic displacements associated with a variety of non-graphitic bonds. To obtain more precise results, this band has been deconvoluted into several bands [35], not always with an explicit method. Most of the authors have deconvoluted up to four curves (D1-D4) and identified each band with a specific interpretation: D1 band with disordered graphitic lattice, D2 band with disordered layers of graphene, D3 band with amorphous carbon, and D4 band with ionic impurities of $sp^3$ bonds [36,37]. To quantify the disorder of soot, the ratio of the integrated intensity of the disordered-induced D-band ($I_D$) and the Raman-allowed G-band ($I_G$) can be used [34]. The parameters obtained for Raman spectra that are correlated with the degree of graphitization have been determined in multiple ways, making it difficult to compare results [38]. However, all studies conclude that a decrease in the $I_D/\ I_G$ ratio implies an increase in the degree of graphitization of carbonaceous materials.

Regarding the identification of the $sp^3$ content, when analysing highly oriented graphite and pure diamond, the peaks are located at 1580 $cm^{-1}$ [35,39] and 1332 $cm^{-1}$ [40,41], respectively. Contrary to the graphite peak, the diamond peak cannot be detected in a soot spectrum, due to the overlap with the D-band [41,42,84]. Some authors have interpreted the existence of an additional peak usually denominated T or D5 (which shifts with wavelength between 1060 and 1150 $cm^{-1}$), hardly noticeable in most soot spectra, associated with $sp^3$ bonds [43]. Due to the difficulty to distinguish this peak from the D band in the visible range, authors have used deep UV excitation, 244 nm or 5.1 eV, where this peak is shifted down to 1050 $cm^{-1}$ [44], thus avoiding overlap with D-band. However, there is no evidence of $sp^3$ being linked to the T-peak [44].

Furthermore, the average crystal length ($L_a$) can also be estimated from Raman spectroscopy. The crystal length is linearly proportional to $I_G/I_D$ [45] with a proportionality constant of 4.4 nm [46,47,85]. This expression is not valid for very small $L_a$ values and an inverse quadratic relationship between $L_a$ and $I_G/I_D$ with a transition point between the two regimes for $L_a = 2$ nm was also proposed [33,86].

X-ray Photoelectron Spectroscopy is a technique based on atomic excitation, which can also be used to characterize the chemical structure of soot [23]. In Fig. 1c typical XPS spectra of soot (solid line), graphite (dot-dashed line), and diamond (dashed line) are shown. All of them present a peak in the C1s core level (corresponding to the carbon band), whereas only soot presents a peak in the O1s core level (oxygen band) due to the eventual presence of oxygenated functionalities. If the peak C1s of soot spectrum is deconvoluted into two different contributions, at 284.4 eV and 285.2 eV, the resulting bands can be attributed to $sp^2$ and $sp^3$ bonds, respectively. In addition, a third peak can be observed at 286.5 eV, attributed to some C–O contamination of the samples. The binding energy values of $sp^2$ and $sp^3$ are consistent with the C1s peaks of graphite and diamond, respectively. Therefore, the $sp^3$ content can be assumed to be proportional to the ratio of the corresponding peak area over the total C1s peak area [48,49].

Atomic Force Microscopy (AFM) is a technique based on the mechanical interaction between a hard non-conducting material that interacts with the surface. With this technique, the soot electrical conductivity ($\sigma$) can be measured (Y. Liu [50]; Y. Liu [51]), which can also be related to the nanostructural parameters of soot.

A methodological approach is proposed based on soot nanostructural parameters (obtained with different experimental techniques) to determine its refractive index with the dispersion model. With this aim, the input parameters of the dispersion model have been related to soot nanostructural intermediate parameters, such as the degrees of graphitization and diamantization and the average length of the graphitic crystals, and these intermediate parameters have been related to direct results from soot characterization techniques. This provides the dispersion model proposed here more versatility and generality than previous dispersion models proposed in the literature.

## 2. Dispersion model and parameters involved

The dispersion model describes how the electronic clouds interact with the electromagnetic field. The field $\vec{E}$ distorts the cloud similarly as a spring acting between the nucleus and the electrons (with mass $m_e$). An induced dipole is opposed to the electron displacement $\vec{r}$, generating a harmonic oscillation, which follows the Hooke law:

$$m_e \frac{\partial \vec{r}}{\partial t^2} + m_e\, g \frac{\partial \vec{r}}{\partial t} + m_e\, \omega_{res}{}^2\, \vec{r} = -\, e\, \vec{E} \tag{1}$$

where $g$ is the damping factor, $e$ is the electron charge, $\omega_{res}$ is the resonant frequency, and $t$ is time.

After transforming this equation into the complex frequency domain, determining the induced dipole moment as the product of the displacement and electronic charge, obtaining the polarization by extending the dipole moment to the whole electronic cloud, defining the dielectric constant as a relation between the polarization and the electromagnetic field, and considering that a carbonaceous material has different types of contributing electrons ($n_{total}$), and thus different additive oscillators, expression (2) is obtained as explained in Section S1 of the Supplementary Material.

$$\varepsilon(\omega) = 1 + \frac{e^2}{m_e\, \varepsilon_0} \sum_{j=1}^{n_{total}} \left[ \frac{n_j \left( \omega_{res,j}{}^2 - \omega^2 + i\omega g_j \right)}{\left( \omega_{res,j}{}^2 - \omega^2 \right)^2 + \omega^2 g_j{}^2} \right] \tag{2}$$

where $\varepsilon_0$ is dielectric constant of vacuum. Since graphite-like carbonaceous materials have various types of electrons ($sp^2$ and $p$ hybridized electrons and free conduction electrons), the final expressions for both, the real and the imaginary parts of the dielectric constant, can be written as:

$$\varepsilon_{real}(\omega) = 1 + \frac{e^2}{m_e \varepsilon_0} \sum_{j=1}^{n_b} \frac{n_j \left( \omega_{res,j}{}^2 - \omega^2 \right)}{\left( \omega_{res,j}{}^2 - \omega^2 \right) + \omega^2 g_j^2} - \frac{e^2}{m^*_{e,c} \varepsilon_0} \frac{n_c}{\omega^2 + g_c^2} \tag{3}$$

$$\varepsilon_{img}(\omega) = 1 + \frac{e^2}{m_e \varepsilon_0} \sum_{j=1}^{n_b} \frac{n_j\, g_j}{\left( \omega_{res,j}{}^2 - \omega^2 \right) + \omega^2 g_j^2} - \frac{e^2}{m^*_{e,c} \varepsilon_0} \frac{n_c\, g_c}{\omega^2 + g_c^2} \tag{4}$$

**Table 1**
Constants used in the dispersion model to simulate optical properties of soot and graphite at room temperature and flame temperature.

| Soot | $T$ (K) | Oscillator | $n(e^-/m^3)$ | $g(s^{-1})$ | $\omega_{res}(s^{-1})$ |
|---|---|---|---|---|---|
| Dalzell & Sarofim [21] | 300 | $c$ | $4.06 \cdot 10^{27}$ | $6.00 \cdot 10^{15}$ | – |
| | | 1 | $2.69 \cdot 10^{27}$ | $6.00 \cdot 10^{15}$ | $1.25 \cdot 10^{15}$ |
| | | 2 | $2.86 \cdot 10^{28}$ | $7.25 \cdot 10^{15}$ | $7.25 \cdot 10^{15}$ |
| Lee & Tien [7] | 300 | $c$ | – | $0.54 \cdot 10^{15}$ | – |
| | | 1 | – | – | $1.25 \cdot 10^{15}$ |
| | | 2 | – | $2.53 \cdot 10^{15}$ | $7.25 \cdot 10^{15}$ |
| | 1450 | $c$ | $4.00 \cdot 10^{25}$ | $1.20 \cdot 10^{15}$ | – |
| | | 1 | $4.07 \cdot 10^{27}$ | $5.90 \cdot 10^{15}$ | $1.25 \cdot 10^{15}$ |
| | | 2 | $4.47 \cdot 10^{28}$ | $5.60 \cdot 10^{15}$ | $7.25 \cdot 10^{15}$ |
| Habib & Vervisch [17] | 1450 | $c$ | $7.00 \cdot 10^{24}$ | $1.20 \cdot 10^{15}$ | – |
| | | 1 | $1.67 \cdot 10^{27}$ | $7.00 \cdot 10^{15}$ | $1.25 \cdot 10^{15}$ |
| | | 2 | $1.83 \cdot 10^{28}$ | $7.25 \cdot 10^{15}$ | $7.25 \cdot 10^{15}$ |
| Stagg & Charalampopoulos [18] | 1450 | $c$ | $2.30 \cdot 10^{23}$ | $1.20 \cdot 10^{15}$ | – |
| | | 1 | $3.38 \cdot 10^{27}$ | $7.30 \cdot 10^{15}$ | $1.25 \cdot 10^{15}$ |
| | | 2 | $3.72 \cdot 10^{28}$ | $9.50 \cdot 10^{15}$ | $7.25 \cdot 10^{15}$ |
| Kelesidis & Pratsinis [53] | 1830 | $c$ | $1.10 \cdot 10^{25}$ | $5.56 \cdot 10^{15}$ | – |
| | | 1 | $1.70 \cdot 10^{27}$ | $1.31 \cdot 10^{15}$ | $1.25 \cdot 10^{15}$ |
| | | 2 | $3.17 \cdot 10^{26}$ | $8.34 \cdot 10^{15}$ | $5.91 \cdot 10^{15}$ |
| Graphite | $T$ (K) | Oscillator | $n(e^-/m^3)$ | $g(s^{-1})$ | $\omega_{res}(s^{-1})$ |
| Stagg & Charalampopoulos [18] | 1450 | $c$ | $2.63 \cdot 10^{26}$ | $1.20 \cdot 10^{15}$ | – |
| | | 1 | $1.31 \cdot 10^{28}$ | $6.30 \cdot 10^{15}$ | $1.25 \cdot 10^{15}$ |
| | | 2 | $1.44 \cdot 10^{29}$ | $1.12 \cdot 10^{16}$ | $7.25 \cdot 10^{15}$ |

where the sums are extended to the bound electron types ($n_b$), expressed in number per unit volume, while the conduction electrons (identified with subscript $c$), have been written separately since they have no resonant frequency. The bound electrons are distributed among different oscillators ($n_j$) depending on the range of frequencies at which they become excited, leading to interband optical transitions. Previous studies dealing with graphite-like materials, such as those by Dalzell & Sarofim [21], Lee & Tien [7], Stagg & Charalampopoulos [18], Habib & Vervisch [17], and Kelsidis & Pratsinis [53] have shown that the dispersion model is able to simulate accurately the optical properties of these materials with only two bound-electron oscillators, at 0.82 eV and 4.77 eV, while a third oscillator (at around 14 eV as shown in Taft and Philipp [52]) is not relevant to simulate the optical response in the usual optical range (wavelength above 300 nm). The spectral ranges (expressed as a function of wavelength, energy, and frequency) where each bound oscillator contributes are shown in Fig. 2. All these studies proposed values for the constants, after fitting the dispersion model to their optical measurements for both soot and graphite at two temperatures, corresponding to room and flame conditions, specifically 300 and 1450 K. These values are collected in Table 1.

As observed in Table 1, except in the Dalzell & Sarofim proposal, relatively low values were proposed for the contributing number of conduction electrons in all cases. Lee & Tien [7] concluded, from the spectral optical properties of graphite described by Taft & Philipp [52], that only a twelfth of the carbon electrons contributed to the first oscillator and extended this conclusion to flame soot. This rule was assumed by other authors using the dispersion model for soot [17,18], as can be checked in Table 1 for both soot and graphite. However, this assumption has been revised.

The number of electrons per unit volume contributing to the optical properties of soot can be estimated from the integration of the imaginary part of the dielectric constant along the wavelength range of each oscillator, following the method proposed by Taft & Philipp [52], combined with the method proposed by Egerton [54] for the estimation of the electronic density considering the Bethe $f$-sum rule [55]:

$$n_1 = \frac{8\pi\varepsilon_0 m_e}{n_{at}\, e^2} \int_0^{\omega_{res1}} f\, \varepsilon_{img} \mathrm{d}f;\; n_2 = \frac{8\pi\varepsilon_0 m_e}{n_{at}\, e^2} \int_{\omega_{res1}}^{\omega_{res2}} f\, \varepsilon_{img} \mathrm{d}f \tag{5}$$

with $n_{at}$ being the atomic density ($m^{-3}$). The combination of both methods is described in the Supplementary Material (Section S2). From the results obtained using the spectral dielectric constants, it can be observed that the number of carbon electrons contributing to the first oscillator is much less than a twelfth, differently to graphite.

In equations (3) and (4), the mass of the conduction electrons ($m^*_{e,c}$) is not the actual electron mass, but an effective mass, lower than the actual one, because these electrons do not have a perfect oscillating movement but a transverse displacement along the basal plane, thus providing electric conductivity to the material. It has been proven that the higher the electric conductivity, the lower the effective mass required to fit the dispersion model. Since the dispersion model is actually a simplification, this effective mass is different from the actual mass of an electron ($m_e$) and is expressed as a constant $b$ times this mass (expression (6)).

$$m^*_{e,c} = b \cdot m_e \tag{6}$$

Constant $b$ is a function of the electronic structure of the material and is referred to as the effective mass factor of conduction electrons. To determine the value of $b$, some authors have proposed different methods. Lee & Tien [7] determined the effective mass by considering that the energy surfaces are ellipsoids of revolution with transverse ($m_t$) and longitudinal ($m_l$) masses [56] with expression (7), based on the average of the different effective axial masses.

$$m^*_{e,c} = 3\left(\frac{1}{m_l} + \frac{2}{m_t}\right)^{-1} \tag{7}$$

Among carbon allotropic varieties, graphite is the main reference for soot, since this is mainly composed of $sp^2$ carbon atoms. However, some studies have proved that soot may also have limited amounts of $sp^3$ carbon atoms [22,57,58]. The presence of these carbon atoms affects different properties of soot such as its electric conductivity. For this reason, diamond can also be considered as a secondary reference for soot. The studies by Lee & Tien [7], Wallace [59], and Schneider [60], using diverse methods, have shown that the effective mass of high-quality graphite crystals is equivalent to $1/18 \approx 0.056$ of the real electron mass, in good agreement with cyclotron resonance measurements [61]. This value is consistent with more specific values proposed for mesoscopic synthetic graphite ($0.052 \pm 0.002$) and for high quality graphite crystals (0.057) [62]. The effective mass factor of the diamond conduction electrons is around 0.47, calculated with expression (7) with the values of the transverse and longitudinal effective masses proposed by Willantzen et al. [63] ($m_t = 0.34\, m_e$ and $m_l = 1.5\, m_e$, resulting in $b =$

**Table 2**
Degree of graphitization for each reference.

| Material | Reference | $G$ | $T$ (K) |
|---|---|---|---|
| **Soot** | Chang & Charalampopoulos | 0.508 | 300 |
| | Dalzell & Sarofim | 0.785 | |
| | Stagg & Charalampopoulos | 0.365 | 1450 |
| | Lee & Tien | 0.543 | |
| | Habib & Vervisch | 0.365 | |
| | Kelesidis & Pratsinis | 0.551 | 1830 |
| **Graphite** | Djurisic & Li | 1.031 | 300 |
| | Stagg & Charalampopoulos | 1.003 | 1450 |

0.459) and by Löfas et al. [64] ($m_t = 0.34\ m_e$ and $m_l = 1.4\ m_e$, resulting in $b = 0.478$).

Nevertheless, some authors have proposed different ways for determining the effective mass of the conduction electrons. Wallace [59] proposed expression (8) to consider its dependence with the electric conductivity, where $kT$ at room temperature is 0.025 eV, the initial band division ($\gamma_0$) is 0.9 eV, and $a_0$ is the in-plane lattice graphite constant, equivalent to 0.246 nm. Schneider [60] theoretically predicted the effective mass based on the principal band division ($\gamma_1$) with expression (9). In both equations $h$ is the Planck constant.

$$m^*_{e,c} = \frac{h^2\ kT}{36\ (\log 2)\ a_0^2\ \gamma_0^2} m_e \tag{8}$$

$$m^*_{e,c} = \frac{4\ h^2\ \gamma_1}{3\ a_0^2\ \gamma_0^2} m_e \tag{9}$$

Contrary to the resonant frequencies of the two bound-electron oscillators, $\omega_{res1}$ and $\omega_{res2}$, which have been almost-consensually fixed at $1.25{\cdot}10^{15}$ $s^{-1}$ and $7.25{\cdot}10^{15}$ $s^{-1}$, respectively (see Table 1 and Fig. 2), very different values have been proposed for the corresponding damping factors, $g_1$ and $g_2$. Differently to these damping factors, the damping factor associated with the conduction electrons (see equations (3) and (4)), does not represent the damping of an oscillator, since it models conduction electrons. Dalzell & Sarofim [21] suggested that this damping factor should be estimated from the mean free path ($l$) of the conduction electrons in graphite, although they did not specify the procedure. The mean free path is the average distance over which a moving particle (such as an electron) travels before substantially changing its direction or energy. The more collisions an electron has, the lower the mean free path and the higher the damping factor, indicating higher resistance to electron mobility. Specifically, Lee & Tien [7] employed expression (10) (where $k_B$ is the Boltzmann constant), initially proposed from Dunlap's study [65]. This relationship was also assumed by Habib & Vervisch [17] in their study. In this expression, the damping factor of the conduction electrons depends on the square root of the temperature, besides being inversely proportional to the mean free path.

$$g_c = \frac{3}{4}\left(\frac{2\pi{\cdot}k_B{\cdot}T}{m^*_{e,c}}\right)^{0.5}\frac{1}{l} \tag{10}$$

There is no consensus for the mean free path of conduction electrons in soot, due to the variability in the structure of this material. Azzolini et al. [66] used three different models of the energy loss function (ELF) to calculate the Inelastic Mean Free Path (IMFP) of diamond and graphite. Results obtained from these models were compared to calculations performed using the Tanuma-Powell-Penn (TPP) model [67] and showed strong agreement, particularly in cases involving energy transfers higher than 100 eV. However, estimations showed significant discrepancies for energies below 100 eV, and no data were proposed for energies below 10 eV. A simpler relationship was proposed decades before by Lee & Tien [7], who suggested that the mean free path should be related to the length of the graphitic crystals ($L_a$) through which the conduction free electrons travel, and specifically proposed half of the average $L_a$:

$$l = \frac{L_a}{2} \tag{11}$$

More specifically, Lee & Tien [7] proposed a value of 1 nm, arguing that the average length of such packages can be of the order of 2 nm. However, the reliability of this data is limited, since other studies have shown, based on X-ray diffraction spectroscopy, that the length of graphitic packages is very variable ([68] shown values around 2.75 nm) and can be much longer, reaching values of up to 5.5 nm [69] and even up to 8 nm in very graphitic soot [70].

It has been discussed that the refractive index is quite insensitive to temperature within the range of flame temperatures [7,18]. On the contrary, there are appreciable differences between the optical properties of flame soot and soot aerosols at room temperature [7]. Since the effect of increasing damping factors of bound electrons is to increase the amplitude of the bands observed in the dielectric constant spectrum [71] (the damping factors can be estimated as half of the width at half height of the oscillation bands) and larger oscillations phases have been observed for higher temperatures [7], it can be concluded that the damping factors should increase with temperature, as also observed in expression (10) for the damping factor of conduction electrons.

## 3. Estimation of the dispersion model parameters

As mentioned before, to apply the dispersion model the following parameters are necessary: the number of electrons of the bonding oscillators ($n_j$), the number of conduction electrons ($n_c$), the bonding ($g_j$) and free damping factors ($g_c$), and the resonant frequencies ($\omega_{res}$). In this section, specific relationships are proposed to characterize the number of electrons and the damping factors, while consensual values have been assumed for the resonant frequencies.

Based on the observation by Lee & Tien [7] about the relationship between $n_1$ and the total number of electrons (assumed here as $n_1 + n_2$, since the contribution of $n_c$ is minor) and on the evidence that this relationship is much lower for soot, expression (12) is proposed to relate the degree of graphitization of soot ($G$) with the number of electrons $n_1$ and $n_2$:

$$\frac{n_1}{n_1+n_2}(\text{soot}) = G\frac{n_1}{n_1+n_2}(\text{graphite}) = \frac{G}{12} \tag{12}$$

Therefore, the number of electrons of the first oscillator depend on the second oscillator, based on the expression (12):

$$n_1 = \frac{n_2{\cdot}G}{12-G} \tag{13}$$

Measurements of electric conductivity with atomic force microscopy [60], with previous thermophoretic or electrostatic sampling, would allow for more precise determination of the number of conduction electrons. Considering that the electric conductivity of graphite in the direction parallel to the basal plane is estimated in the range 2000–3000 $Scm^{-1}$ [72], and that the conductivity of mature flame soot (identified as reference soot) is around 200 $Scm^{-1}$ [50], equation (14) could be used instead, with electric conductivity in $Scm^{-1}$. The selection of an exponential trend is based on the evidence shown by [50] that the logarithm of electric conductivity varies linearly with all the soot internal parameters. A detailed explanation of the procedure is explained in Section S3 in the Supplementary Material.

$$n_c = e^{53.18+3.06{\cdot}10^{-3}{\cdot}\ \sigma} \tag{14}$$

To determine the damping factor of conduction electrons, expression (10) is proposed. However, the value of constant $b$ must be known to calculate the effective mass of conduction electrons (equation (6)). Therefore, the following expression is proposed, based on the fact that more ordered structures (either $sp^2$ or $sp^3$) lead to higher effective mass of the conduction electrons, and assuming linear contributions for both the degree of graphitization ($G$) and the degree of diamantization ($D$).

**Table 3**
Optimized values of the dispersion model parameters for soot and graphite at two temperatures and different graphitization factors.

| Material | $T$ (K) | $G$ | $n_c$ ($e^-/m^3$) | $n_2$ ($e^-/m^3$) | $g_1$ ($s^{-1}$) | $g_2$ ($s^{-1}$) |
|---|---|---|---|---|---|---|
| **Soot** | 300 | 0.65 | $1.22{\cdot}10^{25}$ | $3.99{\cdot}10^{28}$ | $2.95{\cdot}10^{15}$ | $9.77{\cdot}10^{15}$ |
| | 1450 | 0.42 | $1.42{\cdot}10^{25}$ | $3.69{\cdot}10^{28}$ | $4.83{\cdot}10^{15}$ | $9.69{\cdot}10^{15}$ |
| **Graphite** | 300 | 1 | $1.62{\cdot}10^{26}$ | $1.78{\cdot}10^{29}$ | $2.68{\cdot}10^{15}$ | $9.36{\cdot}10^{15}$ |
| | 1450 | | $1.52{\cdot}10^{26}$ | $1.41{\cdot}10^{29}$ | $3.65{\cdot}10^{15}$ | $1.02{\cdot}10^{16}$ |

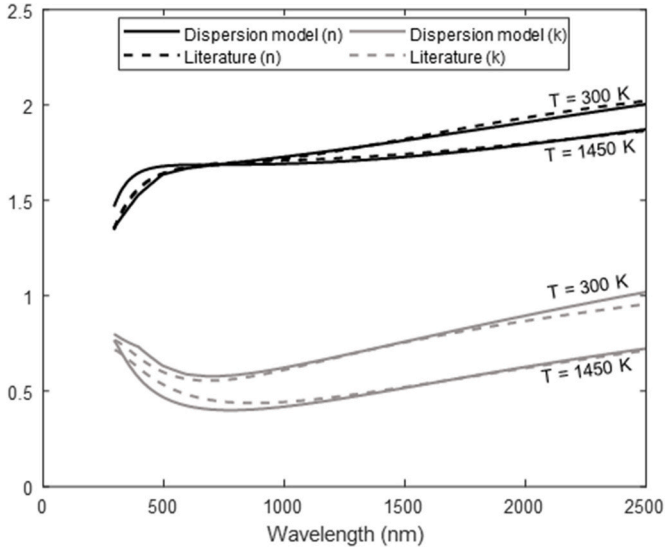


**Fig. 3.** Comparison between results of the proposed model and the average of those proposed in the literature for the real and imaginary parts of the refractive index of soot, for two different temperatures and an average degree of graphitization.

$$b = 0.057{\cdot}G + 0.48{\cdot}D \tag{15}$$

The integral of the spectral imaginary part of the dielectric constant (expression (5)) has been calculated for the different spectral refractive index proposed for soot and graphite in the literature, either through the dispersion model -see Table 1- or through specific correlations or spectral sets of data, such as those proposed by Chang & Charalampopoulos [14] and Djurišić & Li [73], to determine the degree of graphitization ($G$) through expression (12). This yields to the results shown in Table 2.

Nevertheless, the group of parameters proposed in Table 1 do not follow consistent trends with neither temperature ($T$) nor degree of graphitization ($G$) as shown in Lee & Tien [7] with appreciable deviation of the refractive index obtained with the dispersion model from flame to room temperature values. For this reason, new $T$ and $G$ dependent parameters consistent with the expected trends have been determined for $n_c$, $n_2$, $g_1$, and $g_2$, since $n_1$ and $g_c$ can be determined with expressions (13) and (10), respectively. The values for these parameters were selected minimizing the mean squared error between the refractive indices obtained with the dispersion model using the parameters suggested by these authors (averaged for soot at the two available temperatures) and the parameters proposed here. The optimized parameters are shown in Table 3. A detailed explanation of the procedure is explained in Section S4 in the Supplementary Material.

Using the parameters shown in Table 3, the following expressions are proposed to determine the input parameters of the dispersion model based on the temperature and the degree of graphitization.

The number of conduction electrons can be determined with expression (14) based on the conductivity of soot. However, in case that the conductivity of soot is not available, an expression based on the dependence with $T$ and $G$ is proposed. The number of electrons of the second oscillator and the number of conduction electrons depend linearly on temperature and exponentially on the degree of graphitization, and thus, expressions (16) and (17) are proposed for $n_c$ and $n_2$, respectively.

$$n_c(G,T) = a_1\,(1450 - T){\cdot}e^{a_2{\cdot}G} + a_3\,(T - 300){\cdot}e^{a_4{\cdot}G} \tag{16}$$

$$n_2(G,T) = b_1\,(1450 - T){\cdot}e^{b_2{\cdot}G} + b_3\,(T - 300){\cdot}e^{b_4{\cdot}G} \tag{17}$$

The resulting expressions (using the parameters of Table 3) are equation (18) for the number of conduction electrons and equation (19) for the number of electrons involved in the second oscillator.

$$n_c(G,T) = 8.771{\cdot}10^{19}\,(1450 - T){\cdot}e^{7.383{\cdot}G} + 2.215{\cdot}10^{21}\,(T - 300){\cdot}e^{4.090{\cdot}G} \tag{18}$$

$$n_2(G,T) = 2.143{\cdot}10^{24}\,(1450 - T){\cdot}e^{4.282{\cdot}G} + 1.217{\cdot}10^{25}\,(T - 300){\cdot}e^{2.308{\cdot}G} \tag{19}$$

No analytical equation was found to determine the damping factor of the bounded electrons. Therefore, expression (20) is proposed, based on the idea of using the plasma frequency ($\omega_p$) as a limit for the mobility of electrons [56], and considering the dependence with the resonance frequency, the number of electrons per unit volume, the degree of graphitization, and the temperature. Moreover, to simulate the decreasing differences in optical properties as temperature increases, the damping factors should follow an exponential equation with exponents lower than unity.

$$g_j(\omega_{res}, n_j, G, T) = \frac{k_B{\cdot}T^{\alpha_T}}{h{\cdot}{\omega_{res}}^{\alpha_\omega}}\sqrt{\frac{n_j{\cdot}e^2}{m_e{\cdot}\varepsilon_0}} \tag{20}$$

In addition, the temperature and the resonance frequency also depend on the number of electrons per unit volume and on the degree of graphitization in a linear – linear relationship (expressions (21) and (22)).

$$\alpha_T(n_j, G) = u_1 + u_2\cdot G + n_j{\cdot}(u_3 + u_4\cdot G) \tag{21}$$

$$\alpha_\omega(n_j, G) = y_1 + y_2\cdot G + n_j{\cdot}(y_3 + y_4\cdot G) \tag{22}$$

To determine the expressions for $\alpha_T$ and $\alpha_\omega$, the system of equations is solved with a matrix system of type $A\cdot X = B$, where $A$ is the coefficient matrix, $B$ the independent vector, and $X$ the unknown vector ($u_1$, $u_2$, $u_3$, $u_4$, $y_1$, $y_2$, $y_3$, and $y_4$). By operating the system and using a numeric computing platform, the following solutions were found (expressions (23) and (24)).

$$\alpha_T(n_j, G) = -0.1529 + 0.439\cdot G + n_j{\cdot}(-3.5986\cdot10^{-29} + G\cdot3.6312\cdot10^{-29}) \tag{23}$$

$$\alpha_\omega(n_j, G) = 0.5953 + 0.1674\cdot G + n_j{\cdot}(-7.2558\cdot10^{-30} + G\cdot7.0726\cdot10^{-30}) \tag{24}$$

As shown in Fig. 3, the optimized model agrees reasonably well with the average results of the real and imaginary parts of the refractive index of soot obtained from other dispersion models proposed in the literature (listed in Table 2) for the same temperatures and similar degree of graphitization.

## 4. Estimation of the intermediate parameters

In this section, different expressions are proposed to determine the intermediate parameters which relate the dispersion model parameters to the nanosctructural parameters. Fig. 4 shows the relationships between the experimental techniques (blue box), the nanostructure (green

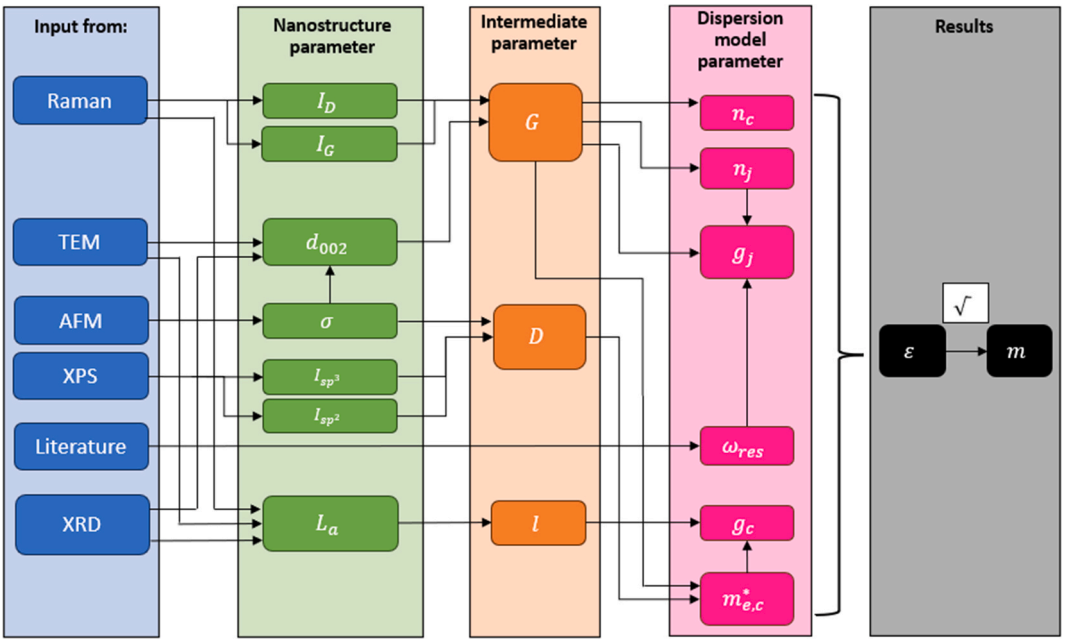


**Fig. 4.** Diagram of the relationships between the experimental techniques, the nanostructure, and the intermediate parameters that allows calculating the dispersion model parameters. The dispersion model parameters $n_c$, $n_j$, $g_c$, and $g_j$ are also affected by the temperature.

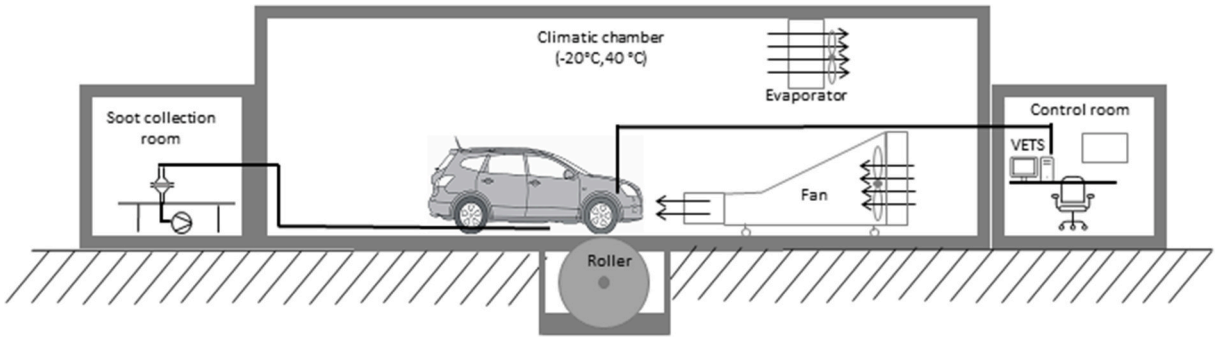


**Fig. 5.** Scheme of the experimental setup including chassis dynamometer, climatic chamber, and soot collection system.

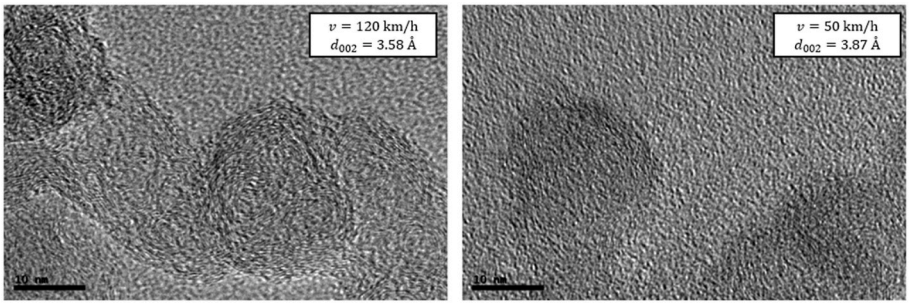


**Fig. 6.** Extreme values of the interlayer distance obtained among all HRTEM images (minimum value for 120 km/h and minimum value for 50 km/h).

box), and the intermediate parameters (orange box) proposed to determine the dispersion model parameters (pink box). The nanostructural parameters can be obtained from a variety of experimental techniques.

The degree of graphitization ($G$) can be obtained either directly from Raman spectroscopy results or through the interlayer distance obtained from HRTEM or from XRD. In case that only results from Raman analysis are available, equation (25) is proposed to evaluate the intensity of the $I_G$ band with respect to the total intensity, considering $I_G$ and $I_D$ bands.

$$G\,(\text{Raman}) = \frac{I_G}{I_G + I_D} \tag{25}$$

However, in case that HRTEM or XRD results are available, the degree of graphitization ($G$) can be better estimated through expression (26) (with $d_{002}$ in Å) following the idea of Atria et al. [32]. For pure graphite crystals the value proposed by Belenkov [29] is $d_{002}$ (graphite) = 3.3796 Å. For the maximun interlayer distance the value can be taken from the literature. Measured soot interplanar distances are usually

equal to or higher than 3.7 Å [31,74–76], although higher values than 3.8 Å have been observed [76].

$$G\,(XRD) = G\,(TEM) = \frac{d_{002}(\max) - d_{002}\,(\text{soot})}{d_{002}(\max) - d_{002}\,(\text{graphite})} \tag{26}$$

As an alternative, the interlayer distance can also be estimated from the electric conductivity using the correlation (27), based on the results by Liu et al. [50].

$$d_{002}\,(\text{soot}) = -0.02 \log \sigma + 3.66 \tag{27}$$

The degree of diamantization ($D$) can be obtained either from the ratio between the intensity of the $sp^3$ band with respect to the sum of the intensities of bands $sp^2$ and $sp^3$ (expression (28)), obtained from XPS, or indirectly from the electric conductivity. In case of knowing the electric conductivity, the degree of diamantization can also be calculated using a correlation (obtained from the data by Liu et al. [50] between conductivity and the ratio of $I_{sp^3}/(I_{sp^3} + I_{sp^2})$. Nevertheless, the validity of this correlation (expression (29)) is limited to the range of electrical conductivity of the study, comprised between 0.1 and 237 S/cm.

$$D(XPS) = \frac{I_{sp^3}}{I_{sp^3} + I_{sp^2}} \tag{28}$$

$$D\,(\sigma) = -0.02 \log \sigma + 0.37 \tag{29}$$

Finally, the mean path of the conduction electrons ($l$) can be estimated from the crystal length ($L_a$) through expression (11), which in turn can be estimated from Raman spectroscopy, HRTEM, XRD, or indirectly through the electric conductivity (based on the results by Liu et al. [50] with equation (30), in Å).

$$L_a = 1.84 \log\,(\sigma) + 24.82 \tag{30}$$

## 5. Experimental methodology

To evaluate the proposed method, refractive index results have been obtained from a soot analysis made in an experimental study, where particle matter was collected in particle filters using a vacuum pump from the exhaust tube. The experimental installation is similar to that described in a previous study about morphological and optical properties of soot particles emitted from a vehicle on a chassis dynamometer [77]. The vehicle used as a soot generator (Peugeot 3008 1.6 blueHDi) was a typical conventional European road vehicle whose characteristics are described in detail in Lapuerta et al. [77]. Vehicle tests were made on a chassis dynamometer under stationary velocities. The simulated velocities were within the ranges of the four phases of the WLTC certification cycle: 120, 100, 70, and 50 km/h. Individual soot agglomerates were sampled with an electrostatic sampler and visualized with low resolution TEM (LRTEM) and their images were subject to digital treatment. For the current study, these analyses were complemented with images from high resolution TEM (HRTEM) and spectroscopic techniques (Raman and X-ray diffraction) of bulk soot samples collected under the mentioned vehicle conditions. The extraction system includes the particle filter and vacuum pump assembly through which the samples are obtained for spectroscopic analyses (see Fig. 5, soot collection room). More details about the experimental installation for the vehicle tests and for the analysis of the soot samples are presented in the Supplementary Material, Section S5.

## 6. Results and discussion

The extreme values of interlayer distance (minimum and maximum, 3.58 and 3.87 Å) obtained after HRTEM image processing are shown in Fig. 6, coinciding with high and low velocities (120 and 50 km/h), respectively. Therefore, the conditions of the combustion process appear to affect the degree of graphitization, and, thus, the refractive index. It must be pointed out that the degree of graphitization may vary throughout the same agglomerate. The photograph at 120 km/h in Fig. 6 is a clear example, as it shows that in the periphery of the primary particles the layers are more graphitic than in the center. This radial heterogeneity has also been reported in the literature for soot sampled from flames [78]. In the case of very heterogeneous internal structures, an average refractive index could be calculated with the dispersion model weighting each area by means of effective medium models, although this would require a more detailed, volume-based characterization of the agglomerate from its TEM images.

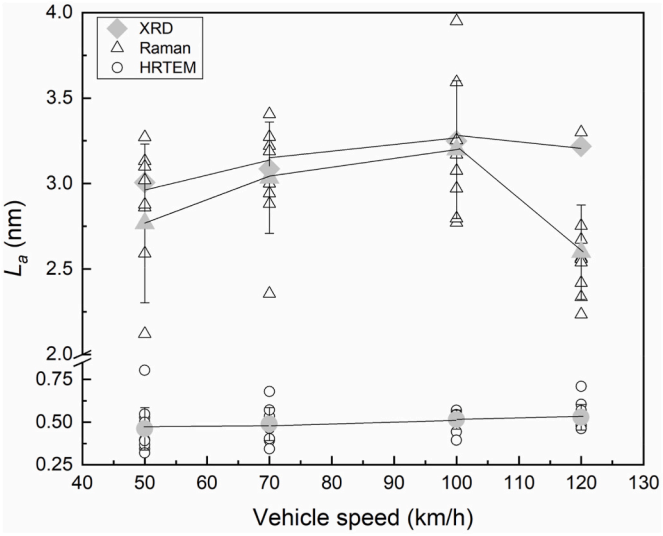


**Fig. 8.** Crystal length in front of vehicle speed, in which the circle icons indicate the HRTEM data, the diamond the XRD, and the triangle the Raman.

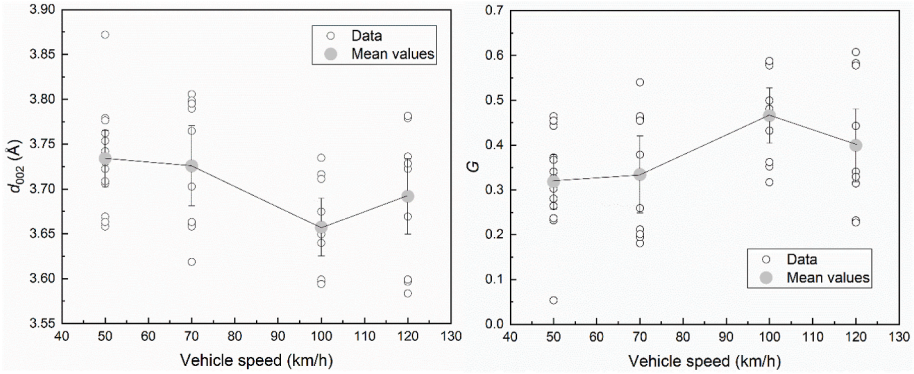


**Fig. 7.** Interlayer distance and degree of graphitization for all HRTEM pictures and the average values in front of vehicle speed.

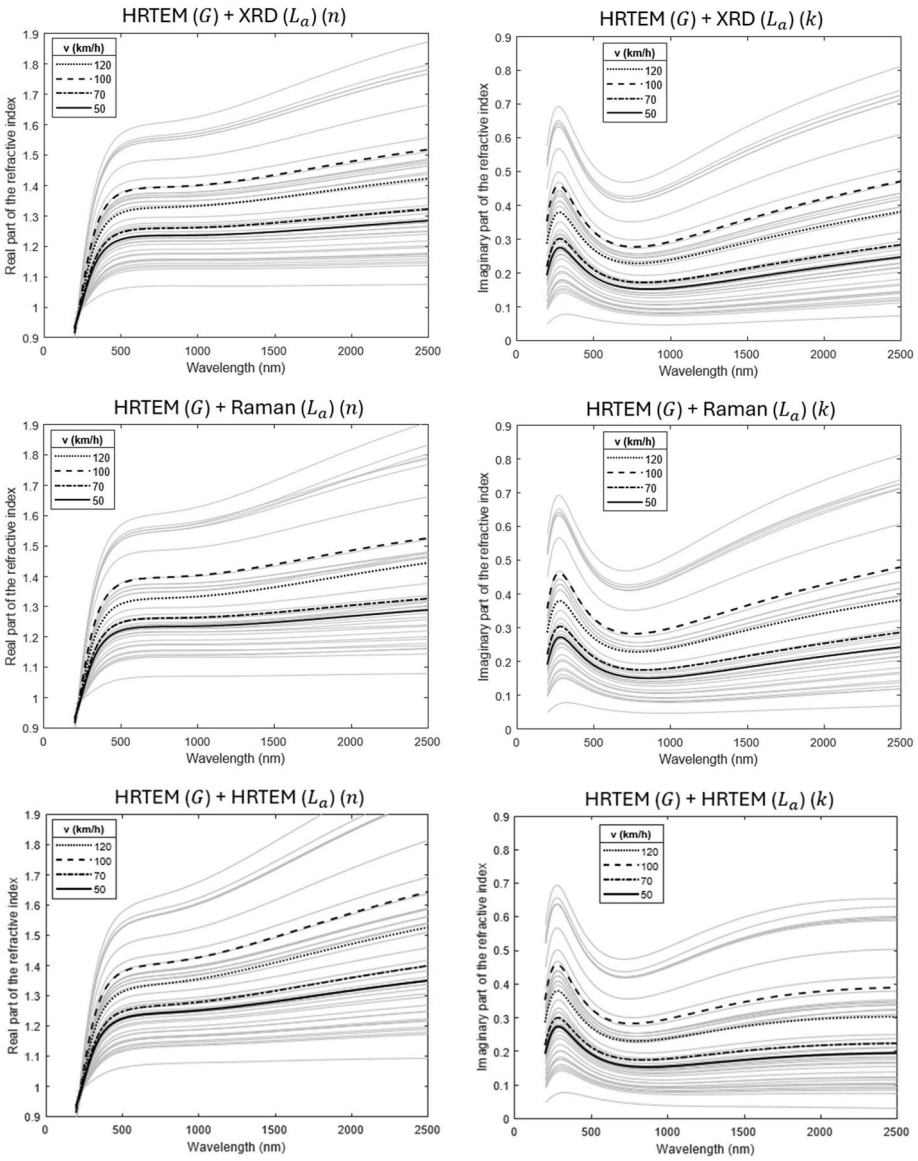


**Fig. 9.** Real and imaginary part of the refractive index for different velocities (120, 100, 70, and 50 km/h) obtained combining the parameters obtained from HRTEM and XRD (top panels), HRTEM and Raman (medium panels), and HRTEM and HRTEM (bottom panels). Grey lines: real and imaginary part for each specific agglomerate. Dark lines: average real and imaginary part for the four velocities.

The degree of graphitization has been determined from the interlayer distance obtained with HRTEM images, with the expression proposed by Atria et al. [32] (equation (25)), considering a maximum interlayer distance of 3.9 Å (above the maximum value obtained in all the pictures analysed). The interlayer distances from HRTEM pictures have been determined with a homemade image processing algorithm which converts the microscopic images into binary images to which a skeletonization procedure is applied [28]. The method is explained in detail in Section S6 of the Supplementary Material. The resulting interlayer distances for all the pictures are shown in Fig. 7 (left) in front of the vehicle speed, together with the calculated degree of graphitization in Fig. 7 (right). The average values and 95 % confidence intervals for the four vehicle speeds are also presented, and their values and trends are consistent with bulk values of the interlayer distance obtained using Bragg's law from XRD spectra (see Supplementary Material, Section S7). As expected, lower interlayer distances lead to higher degrees of graphitization and are within the range of other reported values [28,70,75,76,53]. In addition, as the vehicle speed increases, the observed soot samples have higher degree of graphitization, i.e., the interlayer distances are lower and thus closer to that of graphite, as consequence of the increase in the combustion temperature [79]. This increasing trend is not maintained for 120 km/h probably due to excessive oxidation rate. Although this reversed trend may not be statistically consistent, it could be explained because the average size of primary particles decreases [77] and thus the size of crystals also decreases and the soot becomes less graphitic [80]. A more detailed analysis of the effect of the primary particle diameter on the degree of graphitization, and consequently, on the refractive index, is presented in the Supplementary Material, section S8.

For the application of the dispersion model, the degree of graphitization obtained is complemented with the average crystal length which has been estimated with three different techniques, as shown in Fig. 8: a) XRD, using Scherrer equation, b) Raman, using the equation proposed by Tuinstra & Koenig [45], and c) image processing of HRTEM pictures following the method proposed by Oo et al. [28]. However, any other one of the paths indicated in Fig. 4 could be used depending on the availability of techniques. Specifically, since none of the techniques selected provide reliable information about the degree of

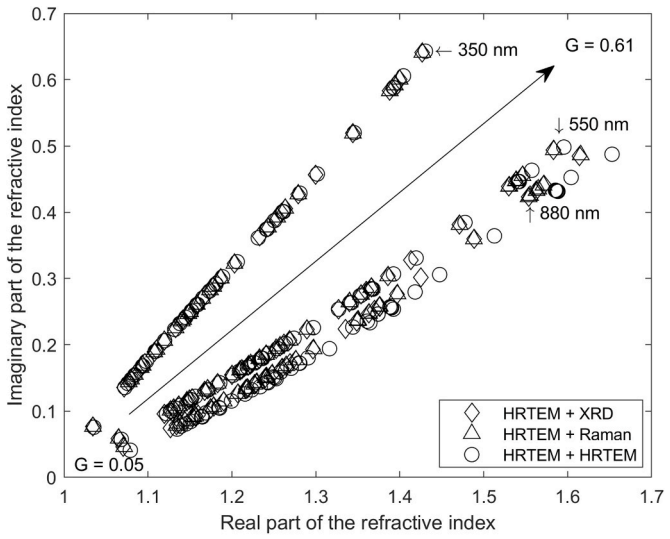


**Fig. 10.** Relationship between the real and imaginary part of the refractive index for three wavelengths (350, 550, and 880 nm) and the three studies: HRTEM + XRD, HRTEM + Raman, and HRTEM + HRTEM.

diamantization, this parameter has not been considered in these examples. The $L_a$ results also show, in general, an increasing trend with vehicle speed for the three techniques used (XRD, Raman, and HRTEM), again except for 120 km/h, probably due to excessive oxidation rate and consequent shrinking of primary particles, as discussed above. The $L_a$ values obtained with spectroscopic techniques are within the range of other reported values [47,81,53]. As observed, the mean crystal length obtained with HRTEM is much lower than that obtained with XRD and Raman, probably because the peaks used from both spectroscopic techniques are mostly affected by the largest crystal lengths (since only consistent patterns in the internal structure lead to visible peaks), whereas in the case of HRTEM skeletization procedure, all crystal sizes are contributing [68]. Another possible source of inaccuracies in HRTEM is the use of two-dimensional projection instead of three-dimensional, although this would not only affect $L_a$ but also $d_{002}$ [68]. In any case, $L_a$ values obtained with HRTEM agree with published results [82,83].

The resulting refractive indices obtained with the dispersion model considering HRTEM and XRD are shown in top panels of Fig. 9, those obtained considering HRTEM and Raman are shown in medium panels, and those obtained from HRTEM and HRTEM (for both $d_{002}$ and $L_a$) are shown in bottom panels. In all cases, refractive indices obtained for each specific HRTEM picture are shown in grey lines along the wavelength range corresponding to significant sunlight radiation, and the average values for each vehicle speed are shown in dark lines with different line codes.

The refractive indices obtained, as well as their trends with increasing wavelength, are within the ranges observed in the literature [7,14–16]. It can be observed that the effect of the selected experimental technique for the determination of the average crystal length is much lower than the variability between soot samples (despite the low $L_a$ values obtained with HRTEM). In the case of using only HRTEM for the nanostructural parameters, notably higher values are reached for the real part of the refractive index at high wavelengths and lower values are obtained for the imaginary part in the same wavelength range. However, these patterns are consequence of the unrealistically low values of the average crystal length. In general, both real and imaginary parts increase with increasing temperature at the combustion chamber (corresponding to increasing vehicle speed).

In all cases, no matter if the crystal length is obtained from XRD, Raman, or HRTEM, the average refractive index obtained (both real and imaginary parts) is higher for increasing degree of graphitization, as observed in [8]. Such increase (from 0.05 to 0.61 in this case) is displayed in Fig. 10, at three wavelength values (350, 550, and 880 nm). The lowest value has been selected to distinguish the effect at UV with enough sunlight radiation intensity. The value of 550 nm has also been selected since it is widely used by many optical measurement equipment and deeply reported in the literature, and 880 nm is the wavelength used to identify the concentration of black carbon from the aethalometer measurements. In addition (as observed in Fig. 9), only slight variations can be observed between the real and imaginary parts of the refractive index using different techniques.

To isolate the effects of the degree of graphitization and that of the average crystal length, computations of the dispersion model were made covering ranges for $G$ and $L_a$ similar to the experimental variability. In the left panel of Fig. 11, it can be observed that increasing the degree of graphitization (keeping the crystal length constant) leads to significant increase in both the real and the imaginary parts of the refractive index (except at very low wavelengths, where only the real part increases). The right panel shows that the effect of increasing the crystal length (with constant degree of graphitization) is minor, and it is only noticeable for wavelengths higher than 1000 nm and for low values of $L_a$.

## 7. Conclusions

The internal structure of soot has been proven to be an essential information to characterize the refractive index with the dispersion model, and therefore to show the different optical behavior of soot agglomerates. Despite high variability can be observed in the individual

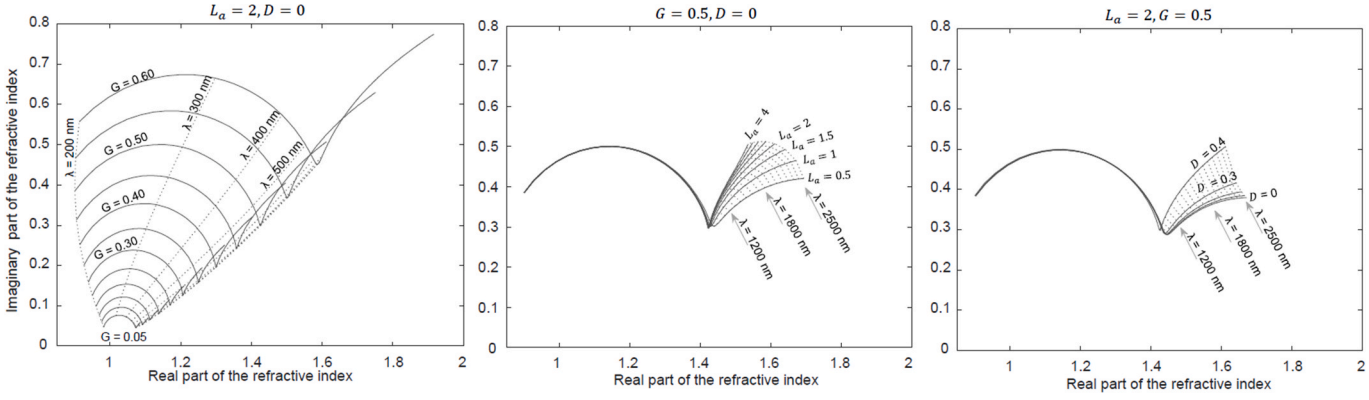


**Fig. 11.** Diagrams with isolines for variable degree of graphitization and constant crystal length and degree of diamantization (left), variable crystal length and constant degrees of graphitization and diamantization (middle), and variable degree of diamantization and constant degree of graphitization and constant crystal length (right). In all cases, wavelength isolines are also displayed.

soot samples, the average interlayer distance between graphene planes decreases and the average crystal length increases with increasing vehicle speed, revealing a slight increase in the degree of graphitization and in the mean free path of conduction electrons, respectively. This behavior is consistent with the increase in the combustion temperature. Among these two characteristics of the internal structure of soot, the degree of graphitization affects the refractive index notably more than the average crystal length. As consequence of this, refractive index results are not highly affected by the technique used to characterize the crystal length, which provides versatility to use the dispersion model depending on the technique available. Nevertheless, among the techniques used for the determination of the crystal length, spectroscopic techniques (XRD or Raman) are preferred to HRTEM, the latter providing much lower results for this structural parameter. In any case, other techniques, apart from HRTEM, Raman, and XRD, can be used to characterize the soot internal structure and chemical composition, such as XPS and AFM, which would allow determining the degree of diamantization (representing the amount of $sp^3$ bonds) and the electric conductivity.

The results obtained from three combinations of techniques (HRTEM for the interlayer distance and XRD for the crystal length, HRTEM for the interlayer distance and Raman for the crystal length, and HRTEM for both), as an example, show that both the real and imaginary parts of the refractive index increase with the degree of graphitization, and are in good agreement with results proposed in the literature. On the contrary, the effect of the average crystal length has been proven to be minor.

The results obtained demonstrate that the refractive index of soot agglomerates (and thus their optical properties and their impact on climate change) is not a universal value but strongly depends on the internal structure of the material, besides depending on the external morphology of the agglomerates, as demonstrated in other studies.

## Availability of data and software

The numerical results and the script of the Matlab software will be available on request.

## CRediT authorship contribution statement

**Sofía González-Correa:** Writing – original draft, Software, Investigation, Data curation. **David Bolonio:** Validation, Methodology, Investigation, Formal analysis, Data curation. **Rosario Ballesteros:** Validation, Supervision, Methodology, Investigation, Formal analysis. **Magín Lapuerta:** Writing – review & editing, Supervision, Resources, Methodology, Formal analysis, Conceptualization.

## Declaration of competing interest

The authors declare the following financial interests/personal relationships which may be considered as potential competing interests: Magin Lapuerta reports financial support was provided by Spain Ministry of Science and Innovation. If there are other authors, they declare that they have no known competing financial interests or personal relationships that could have appeared to influence the work reported in this paper.

## Acknowledgements

The Ministry of Science and Innovation from Spain is gratefully acknowledged by funding the project RAD-SOOT (ref. PID 2019–109767RB-I00). The contract (ref: 2022-UNIVERS-11373) of González-Correa at University of Castilla-La Mancha has been funded by the European Union through European Social Fund Plus (ESF+).

## Appendix A. Supplementary data

Supplementary data to this article can be found online at https://doi.org/10.1016/j.carbon.2024.119426.

## References

[1] T.C. Bond, S.J. Doherty, D.W. Fahey, P.M. Forster, T. Berntsen, B.J. Deangelo, M. G. Flanner, S. Ghan, B. Kärcher, D. Koch, S. Kinne, Y. Kondo, P.K. Quinn, M. C. Sarofim, M.G. Schultz, M. Schulz, C. Venkataraman, H. Zhang, S. Zhang, C. S. Zender, Bounding the role of black carbon in the climate system: a scientific assessment, J. Geophys. Res. Atmos. 118 (11) (2013) 5380–5552, https://doi.org/10.1002/jgrd.50171.

[2] M.Z. Jacobson, W.G. Colella, D.M. Golden, Atmospheric science: Cleaning the air and improving health with hydrogen fuel-cell vehicles, Science 308 (5730) (2005) 1901–1905, https://doi.org/10.1126/science.1109157.

[3] J. Peng, M. Hu, S. Guo, Z. Du, J. Zheng, D. Shang, M.L. Zamora, L. Zeng, M. Shao, Y.S. Wu, J. Zheng, Y. Wang, C.R. Glen, D.R. Collins, M.J. Molina, R. Zhang, Markedly enhanced absorption and direct radiative forcing of black carbon under polluted urban environments, Proc. Natl. Acad. Sci. U.S.A. 113 (16) (2016) 4266–4271, https://doi.org/10.1073/pnas.1602310113.

[4] S.K. Satheesh, K. Krishna Moorthy, Radiative effects of natural aerosols: a review, Atmos. Environ. 39 (11) (2005) 2089–2110, https://doi.org/10.1016/j.atmosenv.2004.12.029.

[5] D.A. Lack, J.M. Langridge, On the attribution of black and brown carbon light absorption using the Ångström exponent, Atmos. Chem. Phys. 13 (20) (2013) 10535–10543, https://doi.org/10.5194/acp-13-10535-2013.

[6] R.P. Bambha, H.A. Michelsen, Effects of aggregate morphology and size on laser-induced incandescence and scattering from black carbon (mature soot), J. Aerosol Sci. 88 (2015) 159–181, https://doi.org/10.1016/j.jaerosci.2015.06.006.

[7] S. Lee, C. Tien, Optical Constants of Soot in Hydrocarbon Flames, The Combustion Institute, 1981, pp. 1159–1166.

[8] T.C. Bond, R.W. Bergstrom, Light absorption by carbonaceous particles: an investigative review, Aerosol. Sci. Technol. 40 (1) (2006) 27–67, https://doi.org/10.1080/02786820500421521.

[9] F. Liu, J. Yon, A. Fuentes, P. Lobo, G.J. Smallwood, J.C. Corbin, Review of recent literature on the light absorption properties of black carbon: refractive index, mass absorption cross section, and absorption function, in: Aerosol Science and Technology, vol. 54, Taylor and Francis Inc, 2020, pp. 33–51, https://doi.org/10.1080/02786826.2019.1676878, 1.

[10] X.U. Zhang, D.J. Faber, A.L. Post, T.G. van Leeuwen, H.J.C.M. Sterenborg, Refractive index measurement using single fiber reflectance spectroscopy, J. Biophot. 12 (7) (2019), https://doi.org/10.1002/jbio.201900019.

[11] J. Mullins, A. Williams, The optical properties of soot: a comparison between experimental and theoretical values, Fuel 66 (2) (1987) 277–280.

[12] D.A.G. Bruggeman, Berechnung verschiedener physikalischer Konstanten von heterogenen Substanzen. III. Die elastischen Konstanten der quasiisotropen Mischkörper aus isotropen Substanzen, Ann. Phys. 421 (2) (1937) 160–178, https://doi.org/10.1002/andp.19374210205.

[13] A. Sihvola, Mixing rules with complex dielectric coefficients, in: Subsurface Sensing Technologies and Applications, vol. 1, 2000. Issue 4.

[14] H. Chang, T.T. Charalampopoulos, Determination of the wavelength dependence of refractive indices of flame soot, Proc. R. Soc. London, A 430 (1880) (1990) 577–591, https://doi.org/10.1098/rspa.1990.0107.

[15] M.G. Flanner, X. Liu, C. Zhou, J.E. Penner, C. Jiao, Enhanced solar energy absorption by internally-mixed black carbon in snow grains, Atmos. Chem. Phys. 12 (10) (2012) 4699–4721, https://doi.org/10.5194/acp-12-4699-2012.

[16] C. Liu, C.E. Chung, Y. Yin, M. Schnaiter, The absorption Ångström exponent of black carbon: from numerical aspects, Atmos. Chem. Phys. 18 (9) (2018) 6259–6273, https://doi.org/10.5194/acp-18-6259-2018.

[17] Z.G. Habib, P. Vervisch, On the refractive index of soot at flame temperature, Combust. Sci. Technol. 59 (4–6) (1988) 261–274, https://doi.org/10.1080/00102208808947100.

[18] B.J. Stagg, T.T. Charalampopoulos, Refractive indices of pyrolytic graphite, amorphous carbon, and flame soot in the temperature range 25° to 600°C, Combust. Flame 94 (4) (1993) 381–396, https://doi.org/10.1016/0010-2180(93)90121-I.

[19] V.R. Stull, G.N. Plass, Emissivity of dispersed carbon particles, J. Opt. Soc. Am. 50 (2) (1960) 121–129, https://doi.org/10.1364/JOSA.50.000121.

[20] R. Starke, G.A.H. Schober, Microscopic theory of the refractive, index Optik 140 (2017) 62–85, https://doi.org/10.1016/j.ijleo.2017.03.088.

[21] W.H. Dalzell, A.F. Sarofim, Optical constants of soot and their application to heat-Flux calculations, J. Heat Tran. 91 (1) (1969) 100–104, https://doi.org/10.1115/1.3580063.

[22] C. Russo, B. Apicella, J.S. Lighty, A. Ciajolo, A. Tregrossi, Optical properties of organic carbon and soot produced in an inverse diffusion flame, Carbon 124 (2017) 372–379, https://doi.org/10.1016/j.carbon.2017.08.073.

[23] M. Lapuerta, J. Rodríguez–Fernández, J. Sánchez-Valdepeñas, Soot reactivity analysis and implications on diesel filter regeneration, Prog. Energy Combust. Sci. 78 (2020), https://doi.org/10.1016/j.pecs.2020.100833.

[24] E. Van Valkenburg, RRUFF: Diamond R050204, 2023. https://rruff.info/Diamond/R050204.

[25] J. Wang, Y. Su, Y. Tian, X. Xiang, J. Zhang, S. Li, D. He, Porous single-crystal diamond, Carbon 183 (2021) 259–266, https://doi.org/10.1016/j.carbon.2021.06.083.

[26] M. Pandey, R. D'cunha, A.K. Tyagi, Defects in CVD diamond: Raman and XRD studies, J. Alloys Compd. 333 (2002). www.elsevier.com/locate/jallcom.

[27] H. Fujimoto, Theoretical X-ray scattering intensity of carbons with turbostratic stacking and AB stacking structures, Carbon 41 (8) (2003) 1585–1592, https://doi.org/10.1016/S0008-6223(03)00116-7.

[28] H.M. Oo, P. Karin, C. Charoenphonphanich, N. Chollacoop, K. Hanamura, Physicochemical characterization of direct injection Engines's soot using TEM, EDS, X-ray diffraction and TGA, J. Energy Inst. 96 (2021) 181–191, https://doi.org/10.1016/j.joei.2021.03.009.

[29] E.A. Belenkov, Formation of graphite structure in carbon crystallites, Inorg. Mater. 37 (9) (2001) 928–934, https://doi.org/10.1023/A:1011601915600.

[30] J. He, jie, Hu, Q. xuan, M. nan Jiang, Q. xing Huang, Nanostructure and reactivity of soot particles from open burning of household solid waste, Chemosphere 269 (2021), https://doi.org/10.1016/j.chemosphere.2020.129395.

[31] P. Parent, C. Laffon, I. Marhaba, D. Ferry, T.Z. Regier, I.K. Ortega, B. Chazallon, Y. Carpentier, C. Focsa, Nanoscale characterization of aircraft soot: a high-resolution transmission electron microscopy, Raman spectroscopy, X-ray photoelectron and near-edge X-ray absorption spectroscopy study, Carbon 101 (2016) 86–100, https://doi.org/10.1016/j.carbon.2016.01.040.

[32] J.V. Atria, F. Rusinko, H.H. Schobert, Structural ordering of Pennsylvania anthracites on heat treatment to 2000-2900°C, Energy Fuel. 16 (6) (2002) 1343–1347, https://doi.org/10.1021/ef010295h.

[33] A.C. Ferrari, J. Robertson, Resonant Raman spectroscopy of disordered, amorphous, and diamondlike carbon, Phys. Rev. B Condens. Matter 64 (7) (2001), https://doi.org/10.1103/PhysRevB.64.075414.

[34] M.S. Dresselhaus, G. Dresselhaus, M.A. Pimenta, P.C. Eklund, Chapter 9: Raman scattering in carbon materials, in: Analytical Applications of Raman Spectroscopy, 1999, pp. 1–492.

[35] A. Sadezky, H. Muckenhuber, H. Grothe, R. Niessner, U. Pöschl, Raman microspectroscopy of soot and related carbonaceous materials: spectral analysis and structural information, Carbon 43 (8) (2005) 1731–1742, https://doi.org/10.1016/j.carbon.2005.02.018.

[36] J.D. Herdman, B.C. Connelly, M.D. Smooke, M.B. Long, J.H. Miller, A comparison of Raman signatures and laser-induced incandescence with direct numerical simulation of soot growth in non-premixed ethylene/air flames, Carbon 49 (15) (2011) 5298–5311, https://doi.org/10.1016/j.carbon.2011.07.050.

[37] A. Baldelli, U. Trivanovic, T.A. Sipkens, S.N. Rogak, On determining soot maturity: a review of the role of microscopy- and spectroscopy-based techniques, in: Chemosphere, vol. 252, Elsevier Ltd, 2020, https://doi.org/10.1016/j.chemosphere.2020.126532.

[38] A.C. Ferrari, J. Robertson, Interpretation of Raman spectra of disordered and amorphous carbon, Phys. Rev. B 61 (20) (2000) 14095–14107, https://doi.org/10.1103/PhysRevB.61.14095.

[39] O. Beyssac, B. Goffé, J.P. Petitet, E. Froigneux, M. Moreau, J.N. Rouzaud, On the characterization of disordered and heterogeneous carbonaceous materials by Raman spectroscopy, Spectrochim. Acta Mol. Biomol. Spectrosc. 59 (10) (2003) 2267–2276, https://doi.org/10.1016/S1386-1425(03)00070-2.

[40] S. Prawer, R.J. Nemanich, Raman spectroscopy of diamond and doped diamond, in: Philosophical Transactions of the Royal Society A: Mathematical, Physical and Engineering Sciences, vol. 362, Royal Society, 2004, pp. 2537–2565, https://doi.org/10.1098/rsta.2004.1451, 1824.

[41] A. Dychalska, P. Popielarski, W. Franków, K. Fabisiak, K. Paprocki, M. Szybowicz, Study of CVD diamond layers with amorphous carbon admixture by Raman scattering spectroscopy, Materials Science- Poland 33 (4) (2015) 799–805, https://doi.org/10.1515/msp-2015-0067.

[42] C. Russo, A. Ciajolo, Effect of the flame environment on soot nanostructure inferred by Raman spectroscopy at different excitation wavelengths, Combust. Flame 162 (6) (2015) 2431–2441, https://doi.org/10.1016/j.combustflame.2015.02.011.

[43] J. Schwan, S. Ulrich, V. Batori, H. Ehrhardt, S.R.P. Silva, Raman spectroscopy on amorphous carbon films, J. Appl. Phys. 80 (1996) 440–447.

[44] A.C. Ferrari, J. Robertson, Origin of the 1150 − cm−1 Raman mode in nanocrystalline diamond, Phys. Rev. B Condens. Matter 63 (12) (2001), https://doi.org/10.1103/PhysRevB.63.121405.

[45] F. Tuinstra, J.L. Koenig, Raman spectrum of graphite, J. Chem. Phys. 53 (3) (1970) 1126–1130, https://doi.org/10.1063/1.1674108.

[46] D.S. Knight, W.B. White, Characterization of diamond films by Raman spectroscopy, J. Mater. Res. 4 (2) (1989) 385–393, https://doi.org/10.1557/JMR.1989.0385.

[47] B. Rohani, C. Bae, Effect of exhaust gas recirculation (EGR) and multiple injections on diesel soot nano-structure and reactivity, Appl. Therm. Eng. 116 (2017) 160–169, https://doi.org/10.1016/j.applthermaleng.2016.11.116.

[48] J. Díaz, G. Paolicelli, F. Salvador, F. Comin, Separation of the sp3 and sp2 components in the C1s photoemission spectra of amorphous carbon films, Phys. Rev. B 54 (11) (1996) 80648069.

[49] P. Merel, M. Tabbal, M. Chaker, S. Moisa, J. Margot, Direct evaluation of the sp 3 content in diamond-like-carbon films by XPS, Appl. Surf. Sci. 136 (1998).

[50] Y. Liu, C. Song, G. Lv, C. Fan, X. Zhang, Y. Qiao, Relationships between the electrical properties and nanostructure of soot particles in a laminar inverse diffusion flame, Proc. Combust. Inst. 37 (1) (2019) 1185–1192, https://doi.org/10.1016/j.proci.2018.06.090.

[51] Y. Liu, C. Song, G. Lv, W. Zhang, H. Chen, Evaluation of the oxidative reactivity and electrical properties of soot particles, Carbon 178 (2021) 37–47, https://doi.org/10.1016/j.carbon.2021.02.086.

[52] E.A. Taft, H.R. Philipp, Optical properties of graphite, Phys. Rev. 138 (1 A) (1965), https://doi.org/10.1103/PhysRev.138.A197.

[53] G.A. Kelesidis, S.E. Pratsinis, Soot light absorption and refractive index during agglomeration and surface growth, Proc. Combust. Inst. 37 (1) (2019) 1177–1184, https://doi.org/10.1016/j.proci.2018.08.025.

[54] R.F. Egerton, Physics of electron scattering, in: Electron Energy-Loss Spectroscopy in the Electron Microscope, Springer US, 2011, pp. 111–229, https://doi.org/10.1007/978-1-4419-9583-4_3.

[55] H. Bethe, Zur Theorie des Durchgangs schneller Korpuskularstrahlen durch Materie, Ann. Phys. 397 (3) (1930) 325–400, https://doi.org/10.1002/andp.19303970303.

[56] T.S. Moss, G.J. Burrell, B. Ellis, Dispersion theory, in: Semiconductor Opto-Electronics, Elsevier, 1973, pp. 23–47, https://doi.org/10.1016/b978-0-408-70326-0.50006-5.

[57] J. Robertson, Diamond-like amorphous carbon, Mater. Sci. Eng. R Rep. 37 (4–6) (2002) 129–281.

[58] C. Russo, B. Apicella, A. Ciajolo, Hydrogen, sp2 carbon Hybridization, and sp2 clustering as Pieces of the Puzzling nanostructure of soot: a closer Look, Energy Fuel. (2023), https://doi.org/10.1021/acs.energyfuels.3c01194.

[59] P. Wallace, The band theory of graphite, Phys. Rev. 11 (9) (1947) 622–634, https://doi.org/10.1103/PhysRev.71.622.

[60] J.M. Schneider, Electronic Properties of Graphite, PhD in Physics, Université Joseph-Fourier, 2010, https://theses.hal.science/tel-00547304.

[61] P. Nozières, Cyclotron resonance in graphite, Phys. Rev. 109 (5) (1958) 1510–1521.

[62] Y. Zhang, J.P. Small, M.E.S. Amori, P. Kim, Electric field modulation of galvanomagnetic properties of mesoscopic graphite, Phys. Rev. Lett. 94 (17) (2005), https://doi.org/10.1103/PhysRevLett.94.176803.

[63] M. Willantzen, M. Cardoua, N.E. Christensen, Linear muffin-tin-orbital and k·p calculations of effective masses and band structure of semiconducting diamond, Phys. Rev. B 50 (24) (1994) 18054–18060, https://doi.org/10.1103/PhysRevB.50.18054.

[64] H. Löfas, A. Grigoriev, J. Isberg, R. Ahuja, Effective masses and electronic structure of diamond including electron correlation effects in first principles calculations using the GW-approximation, AIP Adv. 1 (3) (2011), https://doi.org/10.1063/1.3630932.

[65] W.C. Dunlap, Chapter 4. The electron theory of metals and semiconductors, in: An Introduction to Semiconductors, McGraw Hill, 1957.

[66] M. Azzolini, T. Morresi, G. Garberoglio, L. Calliari, N. Pugno, S. Taioli, M. Dapor, Monte Carlo simulations of measured electron energy-loss spectra of diamond and graphite: role of dielectric-response models, Carbon 118 (2017) 299–309, https://doi.org/10.1016/j.carbon.2017.03.0410008-6223.

[67] S. Tanuma, C. Powell, D. Penn, Calculations of electron inelastic mean free paths. IX. Data for 41 elemental solids over the 50 eV to 30 keV range, Surf. Interface Anal. 43 (2011) 689–713, https://doi.org/10.1002/sia.3522.

[68] Y. Liu, C. Fan, X. Wang, F. Liu, H. Chen, Thermally induced variations in the nanostructure and reactivity of soot particles emitted from a diesel engine, Chemosphere 286 (2022), https://doi.org/10.1016/j.chemosphere.2021.131712.

[69] P. Karin, P. Chammana, P. Oungpakornkaew, P. Rungsritanapaisan, W. Amornprapa, C. Charoenphonphanich, K. Sriprapha, Impact of soot nanoparticle size and quantity on four-ball steel wear characteristics using EDS, XRD and electron microscopy image analysis, J. Mater. Res. Technol. 16 (2022) 1781–1791, https://doi.org/10.1016/j.jmrt.2021.12.111.

[70] M. Lapuerta, F. Oliva, J.R. Agudelo, A.L. Boehman, Effect of fuel on the soot nanostructure and consequences on loading and regeneration of diesel particulate filters, Combust. Flame 159 (2) (2012) 844–853, https://doi.org/10.1016/j.combustflame.2011.09.003.

[71] C.F. Bohren, D. Huffman, Absorption and scattering of light by small particles, in: Absorption and Scattering of Light by Small Particles, Wiley Professional), 1983, https://doi.org/10.1088/0031-9112/35/3/025.

[72] H.O. Pierson, Handbook of Carbon, Graphite, Diamond, and Fullerenes: Properties, Processing, and Applications, 1993.

[73] A.B. Djurišić, E.H. Li, Optical properties of graphite, J. Appl. Phys. 85 (10) (1999) 7404–7410, https://doi.org/10.1063/1.369370.

[74] G.A. Kelesidis, N. Rossi, S.E. Pratsinis, Porosity and crystallinity dynamics of carbon black during internal and surface oxidation, Carbon 197 (2022) 334–340, https://doi.org/10.1016/j.carbon.2022.06.020.

[75] U. Trivanovic, M. Pereira Martins, S. Benz, G.A. Kelesidis, S.E. Pratsinis, Dynamics of soot surface growth and agglomeration by enclosed spray combustion of jet fuel, Fuel 342 (2023), https://doi.org/10.1016/j.fuel.2023.127864.

[76] G.A. Kelesidis, A. Nagarkar, U. Trivanovic, S.E. Pratsinis, Toward Elimination of soot Emissions from jet fuel combustion, Environ. Sci. Technol. 57 (28) (2023) 10276–10283, https://doi.org/10.1021/acs.est.3c01048.

[77] M. Lapuerta, R. Ballesteros, S. González-Correa, Relationships between morphology and optical properties of vehicle-emitted soot, J. Aerosol Sci. 174 (2023), https://doi.org/10.1016/j.jaerosci.2023.106261.

[78] M.L. Botero, Y. Sheng, J. Akroyd, J. Martin, J.A.H. Dreyer, W. Yang, M. Kraft, Internal structure of soot particles in a diffusion flame, Carbon 141 (2019) 635–642, https://doi.org/10.1016/j.carbon.2018.09.063.

[79] H. Marsh, A tribute to Philip L. Walker, Carbon 29 (6) (1991) 703–704, https://doi.org/10.1016/0008-6223(91)90004-3.

[80] M.R. Kholghy, Y. Afarin, A.D. Sediako, J. Barba, M. Lapuerta, C. Chu, J. Weingarten, B. Borshanpour, V. Chernov, M.J. Thomson, Comparison of multiple diagnostic techniques to study soot formation and morphology in a diffusion flame, Combust. Flame 176 (2017) 567–583, https://doi.org/10.1016/j.combustflame.2016.11.012.

[81] R.L.V. Vander Wal, Soot nanostructure: definition, quantification and implications, Journal of Fuels and Lubricants 114 (4) (2005) 429–436.
[82] B. Apicella, P. Pré, M. Alfè, A. Ciajolo, V. Gargiulo, C. Russo, A. Tregrossi, D. Deldique, J.N. Rouzaud, Soot nanostructure evolution in premixed flames by high resolution electron transmission microscopy (HRTEM), Proc. Combust. Inst. 35 (2) (2015) 1895–1902, https://doi.org/10.1016/j.proci.2014.06.121.
[83] C.K. Gaddam, C.H. Huang, R.L. Vander Wal, Quantification of nano-scale carbon structure by HRTEM and lattice fringe analysis, Pattern Recogn. Lett. 76 (2016) 90–97, https://doi.org/10.1016/j.patrec.2015.08.028.
[84] A.C. Ferrari, J. Robertson, Interpretation of Raman spectra of disordered and amorphous carbon, Phys. Rev. B 61 (20) (2000) 14095–14107.
[85] A.C. Ferrari, J. Robertson, Interpretation of Raman spectra of disordered and amorphous carbon, Phyical Reviews B 61 (20) (2000) 14095–14107, https://doi.org/10.1103/PhysRevB.61.14095.
[86] A.B. Palotas, L.C. Rainey, C.J. Feldermann, A.F. Sarofim, J.B. Vander Sande, Soot morphology: an application of image analysis in high-resolution transmission electron microscopy, Microsc. Res. Tech. 33 (3) (1996) 266–278, https://doi.org/10.1002/(SICI)1097-0029(19960215)33:3<266::AID-JEMT4>3.0.CO;2-O.